



Cite this: *Dalton Trans.*, 2014, **43**, 18056

## P(EO-co-LLA) functionalized Fe<sub>3</sub>O<sub>4</sub>@mSiO<sub>2</sub> nanocomposites for thermo/pH responsive drug controlled release and hyperthermia†

Wei Guo,<sup>a</sup> Chunyu Yang,<sup>a</sup> Huiming Lin<sup>\*a,b</sup> and Fengyu Qu<sup>\*a</sup>

The Fe<sub>3</sub>O<sub>4</sub>@mSiO<sub>2</sub> nanocarrier that consisted of a magnetic Fe<sub>3</sub>O<sub>4</sub> nanoparticle core and a mesoporous silica (mSiO<sub>2</sub>) shell was synthesized. It shows a uniform sphere morphology about 65 nm in diameter. Considering the magnetic hyperthermia of Fe<sub>3</sub>O<sub>4</sub> under an alternating magnetic field (AMF), a thermo-sensitive polymer, poly[(ethylene glycol)-co-(L-lactide)] (P(EO-co-LLA)), was used as "gatekeeper" coating outside Fe<sub>3</sub>O<sub>4</sub>@mSiO<sub>2</sub> to regulate the drug release behavior. The design of the nanocarrier was expected to block off the pores at low temperature and to reopen them at high temperature reversibly. The obtained hybrid nanocomposites were capable of loading the anti-cancer drug doxorubicin (DOX) and controlled drug release behavior triggered by the hyperthermia of Fe<sub>3</sub>O<sub>4</sub> under AMF. Besides, the nanocarriers also show pH-sensitive drug release based on the slight differences between the tumor (weakly acid) and the normal tissue (weakly alkaline). What's more, the chemotherapy of DOX combined with magnetic hyperthermia can improve the cytotoxicity obviously. On the basis of the high stability and excellent controlled release performance, the multifunctional nanocarriers exhibit potential applications in targeted-control drug release and hyperthermia for cancer treatment.

Received 11th August 2014,  
Accepted 4th October 2014  
DOI: 10.1039/c4dt02441a

www.rsc.org/dalton

## Introduction

Cancer, which has been regarded as a major cause of mortality worldwide, is a large group of diseases produced by rapid unregulated cell growth. Chemotherapy remains one of the most commonly used methods of many cancer treatments. To improve the therapy effect, nanomedicine has been employed as the platform, showing a good performance. To date, multifunctional nanoparticles, including polymers, micelles, liposomes, dendrimers, ceramics, and even virus capsids, have been used in medical diagnostics, drug delivery, therapy, etc.<sup>1–11</sup> Among these, mesoporous silica nanoparticles (MSNs) have been considered to be the most promising inorganic hosts to store and release drug molecules due to their excellent properties, such as uniform and tunable morphology and pore size, high pore volume and surface area, easily modified surface properties, good biocompatibility and biodegradation.<sup>12–16</sup>

However, without the specific discrimination between normal cells and cancer cells, chemotherapy always induces a huge side effect besides the efficacy. To obtain a smart drug release behavior and beneficial therapy effects, much attention has been focused on the mesoporous silica nanocontainers equipped with "gatekeepers" as the delivery vehicles, in which a regulated drug release at specific time intervals and targeted sites can be achieved by taking advantage of various "gatekeepers".<sup>17–19</sup> Currently, nanoparticles, organic molecules and supramolecular nanovalves have been employed as "gatekeepers" for MSNs, and the controlled release process can be regulated by many special stimuli, such as thermal/electrostatics/magnetic actuation, light, photoirradiation, pH and enzymes.<sup>20–26</sup> For example, using DNA block copolymers as capping agents, Herrmann *et al.* realized light-triggered targeted cargo release.<sup>27</sup> In our previous study, the Konjac oligosaccharide (KOGC) was adopted as the "gatekeeper". Owing to the degradation of the "gate" (KOGC), the cargos can be released triggered by  $\beta$ -mannanase, a normal enzyme in colon of the human body.<sup>28</sup>

Magnetic (Fe<sub>3</sub>O<sub>4</sub> or  $\gamma$ -Fe<sub>2</sub>O<sub>3</sub>) nanoparticles with strong magnetic properties and low toxicity have been widely used as targeted and magnetic resonance imaging agents.<sup>29–31,33</sup> For example, Wang and coworkers synthesized a bicontrollable drug release system with PAH/PSS multilayers on Fe<sub>3</sub>O<sub>4</sub>/mSiO<sub>2</sub>, showing magnetic-targeted and pH-controllable release behav-

<sup>a</sup>Laboratory for Photon and Electronic Bandgap Materials, Ministry of Education, College of Chemistry and Chemical Engineering, Harbin Normal University, Harbin 150025, China. E-mail: qufengyu2013@gmail.com, linhuiming@hrbnu.edu.cn

<sup>b</sup>Institute of Functional Material Chemistry, Faculty of Chemistry, Northeast Normal University, Changchun, 130024, P. R. China

†Electronic supplementary information (ESI) available. See DOI: 10.1039/c4dt02441a

ior.<sup>32</sup> Ultra-small  $\gamma\text{-Fe}_2\text{O}_3$  nanoparticles have also been described as the potential specific positive contrast agents for magnetic resonance molecular imaging.<sup>33–35</sup> Moreover, magnetic nanoparticles can produce localized hyperthermia by hysteresis heating upon exposure to an alternating magnetic field (AMF).<sup>36</sup> When the temperature is raised to 42–45 °C, tumor/cancer cells are damaged or killed due to overheating, while most of the normal cells far away from the magnetic nanoparticles survive.<sup>37,38</sup> At present, there are few reports on the combination of hyperthermia with thermo-sensitive controlled release.<sup>39,40</sup> Vallet-Regí *et al.* synthesized mesoporous silica nanoparticles with iron oxide nanocrystals encapsulated inside the silica matrix and decorated on the surface with a thermoresponsive copolymer of poly(ethyleneimine)-*b*-poly(*N*-isopropylacrylamide) (PEI/NIPAM).<sup>41</sup> Lin and coworkers prepared multifunctional nanocarriers based on the up-conversion luminescent nanoparticles and the thermo/pH-coupling sensitive polymer poly[(*N*-isopropylacrylamide)-*co*-(methacrylic acid)].<sup>42</sup>

Herein, the core-shell nanomaterial ( $\text{Fe}_3\text{O}_4@\text{mSiO}_2$ ), with magnetic  $\text{Fe}_3\text{O}_4$  nanoparticles as the core and mesoporous silica as the shell, was synthesized as the drug loading host. Poly[(ethylene glycol)-*co*-(L-lactide)] (P(EO-*co*-LLA)) was chosen to graft outside  $\text{Fe}_3\text{O}_4@\text{mSiO}_2$  as blocking caps. It is known that P(EO-*co*-LLA) is a typical thermo-sensitive polymer, which exhibits reversible phase transitions between sol and gel in aqueous solution based on the change in temperature.<sup>43</sup> The hyperthermia of  $\text{Fe}_3\text{O}_4$  can serve as the “trigger” to control the “on-off” of the thermo-sensitive polymer which is capable of regulating the drug release. From Scheme 1, firstly,  $\text{Fe}_3\text{O}_4@\text{mSiO}_2$  nanomaterials were synthesized by the typical Stöber method. After the modification of  $\text{Fe}_3\text{O}_4@\text{mSiO}_2$  with -COOH, P(EO-*co*-LLA) can be grafted onto  $\text{Fe}_3\text{O}_4@\text{mSiO}_2$  as the “gatekeeper”. Doxorubicin hydrochloride (DOX) was

adopted as the model to investigate the drug release kinetics of the system. Besides the thermo-sensitive control release behavior triggered by the hyperthermia of  $\text{Fe}_3\text{O}_4$ , the nanocarriers also show pH-sensitive control release based on the slight acidity difference between the tumor and the normal tissue. The magnetic hyperthermia assisted thermo/pH drug release can improve the therapeutic effect on tumor treatment.

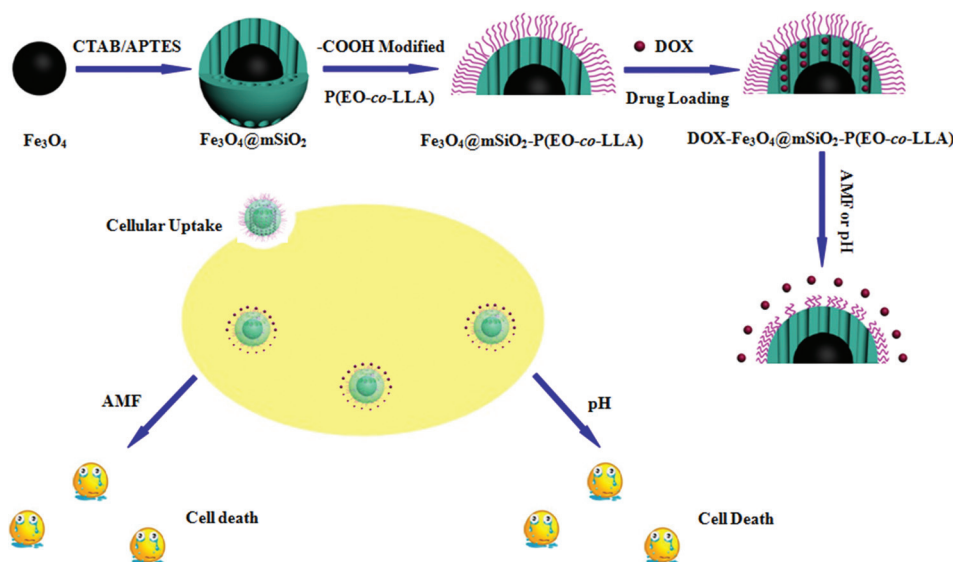
## Experimental section

### Materials

Unless specified, all the chemicals were of analytical grade and were used without further purification. Cetyltrimethylammonium bromide (CTAB), tin(II) 2-ethylhexanoate, 3-aminopropyltriethoxysilane (APTES), tetraethyl orthosilicate (TEOS), 3-[4,5-dimethylthiazol-2-yl]-2,5-diphenyltetrazolium bromide (MTT), 2'-(4-ethoxyphenyl)-5-(4-methyl-1-piperazinyl)-2,5'-bi-1*H*-benzimidazole, trihydrochloride (Hoechst 33342), and monomethoxy poly(ethylene oxide) (PEO,  $M_n \sim 5000$ ) were purchased from Sigma-Aldrich. L-Lactide (LLA) was purchased from Changchun SinoBiomaterials Co. Ltd. Doxorubicin hydrochloride (DOX), sodium oleate and oleic acid were obtained from Aladdin, China. Dimethyl sulfoxide, ferric trichloride hexahydrate ( $\text{FeCl}_3 \cdot 6\text{H}_2\text{O}$ ), ethanol, *n*-hexane and triethylamine were purchased from Tianjin Chemical Corp. of China.

### Synthesis of $\text{Fe}_3\text{O}_4$ nanoparticles

In a typical synthesis of the iron-oleate complex, 10.8 g of iron chloride ( $\text{FeCl}_3 \cdot 6\text{H}_2\text{O}$ , 40 mmol) and 36.5 g of sodium oleate (120 mmol, 95%) were dissolved in a mixture solvent composed of 80 mL ethanol, 60 mL distilled water and 140 mL hexane. The resulting solution was heated to 70 °C and kept at



**Scheme 1** Illustration of the preparation and controlled release process of  $\text{Fe}_3\text{O}_4@\text{mSiO}_2\text{-P(EO-}co\text{-LLA)}$ .

that temperature for four hours. When the reaction was complete, the upper organic layer containing the iron-oleate complex was washed three times with 30 mL distilled water in a separatory funnel. After washing, hexane was evaporated, resulting in an iron-oleate complex in a waxy solid form.

Following a literature procedure,  $\text{Fe}_3\text{O}_4$  nanoparticles were prepared.<sup>44</sup> 36 g (40 mmol) of the iron-oleate and 5.7 g of oleic acid (20 mmol, 90%) were dissolved in 200 g of 1-octadecene (90%) at room temperature. The reaction mixture was heated to 320 °C at a constant heating rate of 3.3 °C min<sup>-1</sup>, and then kept at that temperature for 30 min. When the reaction temperature reached 320 °C, a severe reaction occurred and the initial transparent solution became turbid and brownish black. The resulting solution containing the nanocrystals was then cooled to room temperature, and 500 mL of ethanol was added to the solution to precipitate the nanocrystals, which were further collected by centrifugation and then dispersed in chloroform.

### Synthesis of $\text{Fe}_3\text{O}_4$ @ $\text{mSiO}_2$ nanoparticles

In a typical procedure, 0.5 mL of the  $\text{Fe}_3\text{O}_4$  nanocrystals in chloroform (10 mg mL<sup>-1</sup>) was poured into 8 mL of a 0.2 M aqueous CTAB solution and the resulting solution was stirred vigorously for 30 min. The formation of an oil-in-water microemulsion resulted in a turbid brown solution. Then, the mixture was held at 60 °C for 30 min to evaporate the chloroform, resulting in a transparent black  $\text{Fe}_3\text{O}_4$ /CTAB solution. Then, 20 mL of distilled water was added to the obtained black solution and the pH value of the mixture was adjusted to 8 to 9 using 0.1 M NaOH. After that, 100 µL of 20% TEOS in ethanol was injected six times in 30 min intervals. The reaction mixture was reacted for 24 h under vigorous stirring. The as-synthesized  $\text{Fe}_3\text{O}_4$ @ $\text{mSiO}_2$  NPs were washed three times with ethanol to remove the unreacted species.

### Syntheses of diblock copolymers (P(EO-co-LLA)) with different molecular weights

P(EO-co-LLA)-7250 was synthesized following a literature procedure.<sup>45</sup> PEO (8 g, 1.60 mmol) was added to 80 mL of dried toluene and the residual water in the solution was removed by azeotropic distillation to a final volume of 30 mL. L-Lactide (3.6 g, 25.00 mmol) and stannous octoate (8.7 mg, 21.47 mmol) were added to this PEO/toluene solution and refluxed under a dry nitrogen atmosphere for 24 h. The solution was precipitated in diethyl ether and filtered, and the residual solvent was eliminated by vacuum drying. Diblock copolymers with various molecular weights P(EO-co-LLA)-8750 and P(EO-co-LLA)-10 000 were synthesized by a similar method with 6 g and 8 g of L-lactide. The NMR spectrum of as-synthesized P(EO-co-LLA) is shown in Fig. S1† that testifies the polymerization between PEO and L-lactide.

### Synthesis of $\text{Fe}_3\text{O}_4$ @ $\text{mSiO}_2$ -P(EO-co-LLA)

In a typical procedure, as-synthesized  $\text{Fe}_3\text{O}_4$ @ $\text{mSiO}_2$  nanoparticles (300 mg) were suspended in 20 mL of dry toluene containing 100 µL of APTES. The solution was stirred at 50 °C

under nitrogen for 4 h to obtain amine-functionalized  $\text{Fe}_3\text{O}_4$ @ $\text{mSiO}_2$  ( $\text{Fe}_3\text{O}_4$ @ $\text{mSiO}_2$ -NH<sub>2</sub>). Later on, 200 mg of  $\text{Fe}_3\text{O}_4$ @ $\text{mSiO}_2$ -NH<sub>2</sub> was added into 10 mL DMSO solution containing succinic anhydride (60 mg) and triethylamine (60 mg) and stirred at 40 °C for 48 h to produce the carboxyl-functionalized  $\text{Fe}_3\text{O}_4$ @ $\text{mSiO}_2$  ( $\text{Fe}_3\text{O}_4$ @ $\text{mSiO}_2$ -COOH). 330 mg of  $\text{Fe}_3\text{O}_4$ @ $\text{mSiO}_2$ -COOH was added into 20 mL methylene chloride solution containing 350 mg of dichlorosulfoxide and stirred at 50 °C for 4 h, and then 4.0 g of P(EO-co-LLA) ( $M_n$  = 7250) was added and stirred for another 4 h to obtain  $\text{Fe}_3\text{O}_4$ @ $\text{mSiO}_2$ -P7250. Using P(EO-co-LLA)s with other molecular weights (8750 and 10 000), the samples were named  $\text{Fe}_3\text{O}_4$ @ $\text{mSiO}_2$ -P8750 and  $\text{Fe}_3\text{O}_4$ @ $\text{mSiO}_2$ -P10000.

### Preparation of FITC labeled $\text{Fe}_3\text{O}_4$ @ $\text{mSiO}_2$ -P(EO-co-LLA)

In a typical synthesis of FITC-APTES, 15.6 mg of FITC and 100 µL of (3-aminopropyl)triethoxysilane (APTES) were dissolved in 5 mL DI water. The resulting solution was stirred at room temperature and kept in the dark for 24 hours. FITC-APTES is attached to  $\text{Fe}_3\text{O}_4$ @ $\text{mSiO}_2$ -P(EO-co-LLA) via the reaction among silica coupling groups of FITC-APTES and the residual Si-OH on the silica spheres. In a typical process, 60.0 mg of  $\text{Fe}_3\text{O}_4$ @ $\text{mSiO}_2$ -P(EO-co-LLA) was dispersed in 3 mL of DI water, and then 2 mL of the obtained FITC-APTES solution was added. The reaction was performed in the dark at ambient temperature overnight. The solid was collected by centrifugation, followed by washing 6 times with DI water and freeze drying.

### Drug loading and release

$\text{Fe}_3\text{O}_4$ @ $\text{mSiO}_2$ -P(EO-co-LLA) (60 mg) was added to the DOX solution (3 mL, 1 mg mL<sup>-1</sup>) and stirred at 45 °C for 12 h. Then, the solid was shock cooled, centrifuged, and washed several times with distilled water. The loading amount of DOX was determined by the UV/vis spectroscope at 480 nm, and the drug loading sample was named DOX- $\text{Fe}_3\text{O}_4$ @ $\text{mSiO}_2$ -P(EO-co-LLA). The loading efficiency (LE%) of DOX can be calculated using formula (1). The experiment was repeated three times.

$$\text{LE}\% = \frac{m_{(\text{original DOX})} - m_{(\text{residual DOX})}}{m_{(\text{mSiO}_2)} + m_{(\text{original DOX})} - m_{(\text{residual DOX})}} \times 100\% \quad (1)$$

The gating protocol was investigated by studying the release profiles of DOX from the DOX- $\text{Fe}_3\text{O}_4$ @ $\text{mSiO}_2$ -P(EO-co-LLA) at 25/45 °C in certain media solutions (pH 5.8 or 7.4, phosphate buffer solution). Briefly, 10 mg of DOX loaded  $\text{Fe}_3\text{O}_4$ @ $\text{mSiO}_2$ -P(EO-co-LLA) (DOX- $\text{Fe}_3\text{O}_4$ @ $\text{mSiO}_2$ -P(EO-co-LLA)) was dispersed in 5 mL of media solution and sealed in a dialysis bag (molecular weight cutoff 8000), which was submerged in 20 mL of media solution. At selected intervals, the solution was taken out to determine the release amount by UV. The drug release of DOX from the DOX- $\text{Fe}_3\text{O}_4$ @ $\text{mSiO}_2$ -P(EO-co-LLA) in AMF experiments was performed with a similar method, but the difference is that the drug loading system was put in the AC magnetic field (250 kHz).

### Cell culture

HeLa cells (cervical cancer cell line) were grown in a monolayer of Dulbecco's modified Eagle's medium (DMEM, Gibco) supplemented with 10% (v/v) fetal bovine serum (FBS, Tianhang Bioreagent Co., Zhejiang) and penicillin/streptomycin ( $100 \text{ U mL}^{-1}$  and  $100 \mu\text{g mL}^{-1}$ , respectively, Gibco) under a humidified 5%  $\text{CO}_2$  atmosphere at  $37^\circ\text{C}$ .

### Confocal laser scanning microscopy (CLSM)

To determine the cellular uptake, HeLa cells were cultured in a 12-well chamber slide with one piece of coverglass at the bottom of each chamber in the incubation medium (DMEM) for 24 h. The cell nucleus was labeled with Hoechst 33342.  $\text{Fe}_3\text{O}_4@\text{mSiO}_2\text{-P(EO-co-LLA)}$  was added to the incubation medium at a concentration of  $100 \mu\text{g mL}^{-1}$  for 6 h of incubation in 5%  $\text{CO}_2$  at  $37^\circ\text{C}$ . After the medium was removed, the cells were washed twice with PBS (pH 7.4) and the coverglass was visualized under a laser scanning confocal microscope (FluoView FV1000, Olympus).

### Cell viability

The viability of cells in the presence of nanoparticles was investigated using a 3-[4,5-dimethylthiazol-2-yl]-2,5-diphenyltetrazolium bromide (MTT, Sigma) assay. The assay was performed in triplicate in the following manner. For the MTT assay, HeLa cells were seeded into 96-well plates at a density of  $1 \times 10^4$  per well in  $100 \mu\text{L}$  of the medium and grown overnight. The cells were then incubated with various concentrations of the need tested samples for 48 h. Afterwards, cells were incubated in media containing  $0.5 \text{ mg mL}^{-1}$  of MTT for 4 h. The precipitated formazan violet crystals were dissolved in  $100 \mu\text{L}$  of 10% SDS in 10 mmol HCl solution at  $37^\circ\text{C}$  overnight. The absorbance was measured at 570 nm with a multidetection microplate reader (Synergy<sup>TM</sup> HT, BioTek Instruments Inc., USA).

### Characterization

Powder X-ray patterns (XRD) were recorded on a Siemens D 5005 X-ray diffractometer with Cu  $\text{K}\alpha$  radiation (40 kV, 30 mA). The nitrogen adsorption/desorption, surface areas, and median pore diameters were measured using a Micromeritics ASAP 2010 M sorptometer. The surface area was calculated according to the conventional BET method and the adsorption branches of the isotherms were used for the calculation of the pore parameters using the BJH method. Fourier transform infrared (FTIR) spectra were recorded on a PerkinElmer 580B infrared spectrophotometer using the KBr pellet technique. A UV-vis spectrum was used to describe the amount of drug released (Shimadzu UV2550 spectrophotometer). Transmission electron microscopy (TEM) images were recorded on a TECNAI F20. Zeta potential and dynamic light scattering (DLS) were carried out with a ZetaPALS zeta potential analyzer. The magnetic properties of samples were characterized with a vibrating sample magnetometer (Lake Shore 7410). The alternating mag-

netic field was generated by the alternating magnetic field (Generator-SP04C).

## Results and discussion

### Morphology, structure and phase

TEM was used to display the core-shell structure of the samples (Fig. 1). Fig. 1A shows the TEM image of  $\text{Fe}_3\text{O}_4$  nanoparticles that reveals a uniform and well dispersed spherical morphology with the average diameter of 20 nm in size.

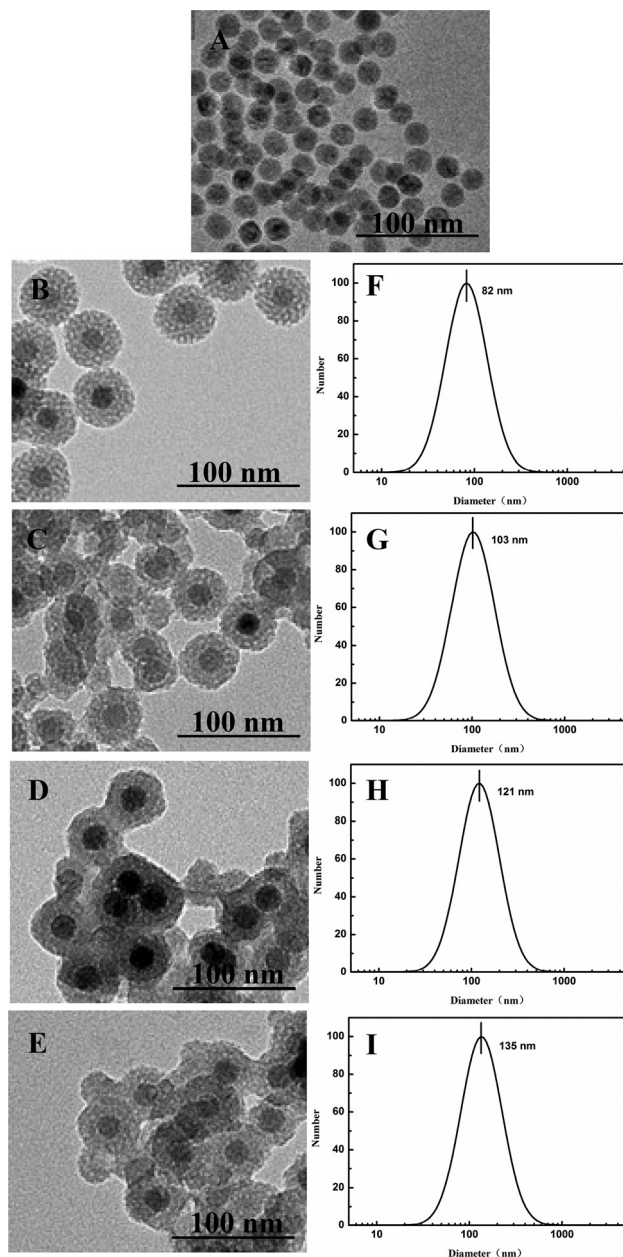


**Fig. 1** TEM images of (A)  $\text{Fe}_3\text{O}_4$ , (B)  $\text{Fe}_3\text{O}_4@\text{mSiO}_2$ , (C)  $\text{Fe}_3\text{O}_4@\text{mSiO}_2\text{-P7250}$ , (D)  $\text{Fe}_3\text{O}_4@\text{mSiO}_2\text{-P8750}$ , (E)  $\text{Fe}_3\text{O}_4@\text{mSiO}_2\text{-P10000}$  and the hydrodynamic size distribution of (F)  $\text{Fe}_3\text{O}_4@\text{mSiO}_2$ , (G)  $\text{Fe}_3\text{O}_4@\text{mSiO}_2\text{-P7250}$ , (H)  $\text{Fe}_3\text{O}_4@\text{mSiO}_2\text{-P8750}$ , and (I)  $\text{Fe}_3\text{O}_4@\text{mSiO}_2\text{-P10000}$ .



$\text{Fe}_3\text{O}_4@\text{mSiO}_2$  shows the obvious core-shell structure with an  $\text{Fe}_3\text{O}_4$  core and a mesoporous silica shell about 20 nm in thickness (Fig. 1B). Through esterification, P(EO-co-LLA) can be grafted onto the surface of  $\text{Fe}_3\text{O}_4@\text{mSiO}_2$ . The polymer layers result in a rough surface and less dispersion of all  $\text{Fe}_3\text{O}_4@\text{mSiO}_2$ -P(EO-co-LLA) nanoparticles (Fig. 1C-E). Additionally, the hydrodynamic diameters of  $\text{Fe}_3\text{O}_4@\text{mSiO}_2$  and  $\text{Fe}_3\text{O}_4@\text{mSiO}_2$ -P(EO-co-LLA)s were measured using a zeta potential analyzer. As illustrated in Fig. 1F, the diameter of  $\text{Fe}_3\text{O}_4@\text{mSiO}_2$  centers at 82 nm is larger than that observed from TEM because of the hydrate layer in the aqueous environment. As depicted in Fig. 1G-I, the diameter of  $\text{Fe}_3\text{O}_4@\text{mSiO}_2$ -P(EO-co-LLA)s increases from 103 nm to 121 and 135 nm with the polymer molecular weight increasing from 7250 to 8750 and 10 000, respectively. The zeta-potential test was further used to monitor the difference between  $\text{Fe}_3\text{O}_4@\text{mSiO}_2$  and  $\text{Fe}_3\text{O}_4@\text{mSiO}_2$ -P(EO-co-LLA)s (Fig. 2). The zeta-potential value increased from  $-16.02 \pm 2.17$  mV for  $\text{Fe}_3\text{O}_4@\text{mSiO}_2$  to  $-2.2 \pm 4.57$  mV for  $\text{Fe}_3\text{O}_4@\text{mSiO}_2$ -P7250. With abundant surface Si-OH, silica always shows the negative charge ( $-16.02 \pm 2.17$  mV). After grafting with P(EO-co-LLA), the decrease of surface Si-OH induces an increase of zeta-potential for  $\text{Fe}_3\text{O}_4@\text{mSiO}_2$ -P(EO-co-LLA).  $\text{Fe}_3\text{O}_4@\text{mSiO}_2$ -P8750 and  $\text{Fe}_3\text{O}_4@\text{mSiO}_2$ -P10000 show a zeta-potential of  $-3.08 \pm 4.17$  mV and  $-4.83 \pm 5.86$  mV, respectively (Fig. 2). Furthermore, with the same addition amount of P(EO-co-LLA), P(EO-co-LLA)-7250 possesses the most molecules to interact with surface Si-OH and to make the highest zeta-potential of all.

Eager to further verify the successful grafting of P(EO-co-LLA) on  $\text{Fe}_3\text{O}_4@\text{mSiO}_2$ , FT-IR spectroscopy was monitored to study the organic and inorganic components of the samples. The corresponding FT-IR spectra of PEO, L-lactide, P(EO-co-LLA),  $\text{Fe}_3\text{O}_4@\text{mSiO}_2$  and  $\text{Fe}_3\text{O}_4@\text{mSiO}_2$ -P(EO-co-LLA) are shown in Fig. 3. As depicted in Fig. 3A, the absorption bands at 2948 and 2887  $\text{cm}^{-1}$  are assigned to the C-H stretching vibrations, and the absorption bands at 1110 and 962  $\text{cm}^{-1}$  can be assigned to the C-O-C stretching vibrations and C-H rocking vibrations of PEO. The obvious absorption band at

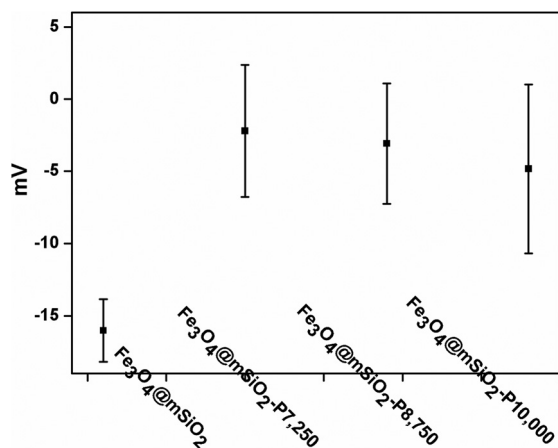


Fig. 2 Zeta-potential of  $\text{Fe}_3\text{O}_4@\text{mSiO}_2$ ,  $\text{Fe}_3\text{O}_4@\text{mSiO}_2$ -P7250,  $\text{Fe}_3\text{O}_4@\text{mSiO}_2$ -P8750 and  $\text{Fe}_3\text{O}_4@\text{mSiO}_2$ -P10000.

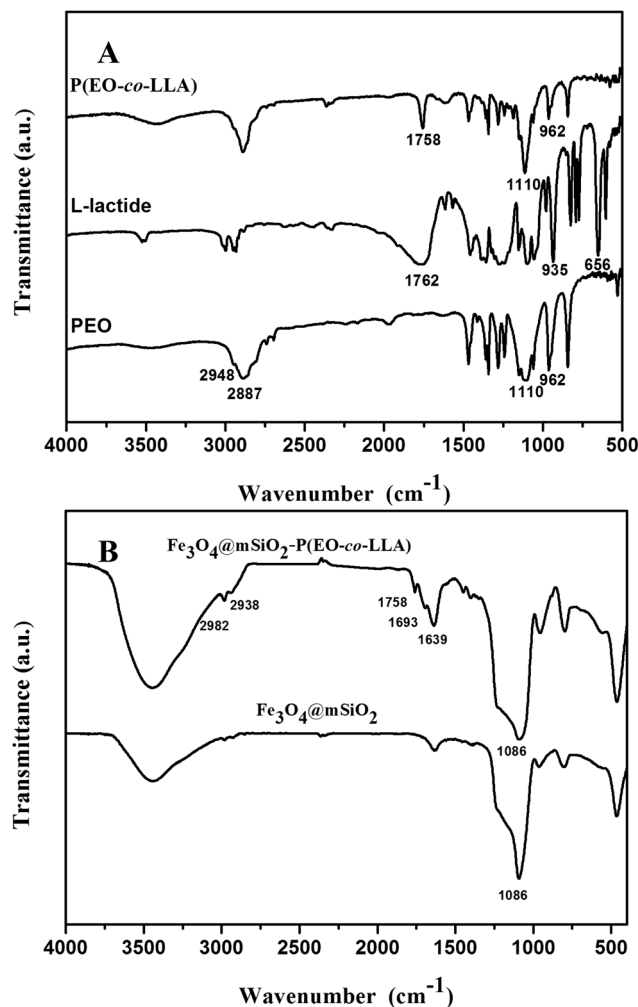


Fig. 3 FTIR spectra of (A) PEO, L-lactide and P(EO-co-LLA); (B)  $\text{Fe}_3\text{O}_4@\text{mSiO}_2$  and  $\text{Fe}_3\text{O}_4@\text{mSiO}_2$ -P(EO-co-LLA).

1762  $\text{cm}^{-1}$  testifies the C=O stretching vibrations of the ester group in L-lactide. In addition, L-lactide also gives the characteristic absorption bands at 935 and 656  $\text{cm}^{-1}$  due to its six-membered ring structure. After the polymerization, P(EO-co-LLA) also shows the stretching vibration adsorption peaks of C=O (1758  $\text{cm}^{-1}$ ) and C-O-C (1110  $\text{cm}^{-1}$ ), but the six-membered rings' characteristic absorption bands (935 and 656  $\text{cm}^{-1}$ ) disappear, testifying the open-ring polymerization of L-lactide. In Fig. 3B, the obvious absorption band at 1086  $\text{cm}^{-1}$  testifies the Si-O-Si framework of  $\text{Fe}_3\text{O}_4@\text{mSiO}_2$ . After P(EO-co-LLA) was grafted, two peaks assigned to C-H stretching vibrations at 2982 and 2938  $\text{cm}^{-1}$  appear. The absorption peaks at 1758, 1693 and 1639  $\text{cm}^{-1}$  assigned to the C=O stretching vibrations of P(EO-co-LLA) can also be found in  $\text{Fe}_3\text{O}_4@\text{mSiO}_2$ -P(EO-co-LLA), confirming that P(EO-co-LLA) has been successfully grafted on  $\text{Fe}_3\text{O}_4@\text{mSiO}_2$ .

The X-ray diffraction patterns (XRD) were collected from  $\text{Fe}_3\text{O}_4@\text{mSiO}_2$  and  $\text{Fe}_3\text{O}_4@\text{mSiO}_2$ -P(EO-co-LLA)s. In Fig. S2,<sup>†</sup> all samples show only one diffraction peak at about  $2\theta = 2.26^\circ$ ,

**Table 1** Pore parameters and loading efficiency of the samples

Samples	BET (m <sup>2</sup> g <sup>-1</sup> )	V <sub>p</sub> (cm <sup>3</sup> g <sup>-1</sup> )	Pore size (nm)	LE (%)
Fe <sub>3</sub> O <sub>4</sub> @mSiO <sub>2</sub>	326	0.285	2.42	—
DOX-Fe <sub>3</sub> O <sub>4</sub> @mSiO <sub>2</sub> -P7250	152	0.156	2.31	5.9 ± 0.4
DOX-Fe <sub>3</sub> O <sub>4</sub> @mSiO <sub>2</sub> -P8750	100	0.133	2.30	6.2 ± 0.6
DOX-Fe <sub>3</sub> O <sub>4</sub> @mSiO <sub>2</sub> -P10000	68.0	0.095	2.30	6.8 ± 0.5

suggesting that they possess the ordered mesoporous structure. It is clearly observed that the relative intensities of the peaks of the pattern collected from Fe<sub>3</sub>O<sub>4</sub>@mSiO<sub>2</sub>-P(EO-co-LLA)s was reduced obviously as compared to that of Fe<sub>3</sub>O<sub>4</sub>@mSiO<sub>2</sub> without P(EO-co-LLA) grafted. Moreover, the larger the amount of P(EO-co-LLA) grafted onto Fe<sub>3</sub>O<sub>4</sub>@mSiO<sub>2</sub>, the lower the diffraction intensity of Fe<sub>3</sub>O<sub>4</sub>@mSiO<sub>2</sub>-P(EO-co-LLA)s, which is consistent with the previous report.<sup>28</sup> The pore structure and related textural properties of Fe<sub>3</sub>O<sub>4</sub>@mSiO<sub>2</sub> and Fe<sub>3</sub>O<sub>4</sub>@mSiO<sub>2</sub>-P(EO-co-LLA)s were followed using nitrogen adsorption-desorption measurements. As can be seen in Fig. S3A,† Fe<sub>3</sub>O<sub>4</sub>@mSiO<sub>2</sub> displays the typical IV adsorption isotherm and a steep capillary condensation step at  $P/P_0 = 0.2-0.4$ . The typical H4 hysteresis loop further testifies the mesoporous structure of Fe<sub>3</sub>O<sub>4</sub>@mSiO<sub>2</sub>.

As depicted in Fig. S3A,† there is a much smaller uptake of nitrogen for Fe<sub>3</sub>O<sub>4</sub>@mSiO<sub>2</sub>-P(EO-co-LLA) taking its counterpart (Fe<sub>3</sub>O<sub>4</sub>@mSiO<sub>2</sub>) as a comparison. Additionally, the surface area ( $S_{\text{BET}}$ ) and pore volume are reduced from 326 m<sup>2</sup> g<sup>-1</sup> and 0.285 cm<sup>3</sup> g<sup>-1</sup> for Fe<sub>3</sub>O<sub>4</sub>@mSiO<sub>2</sub> to 152 m<sup>2</sup> g<sup>-1</sup> and 0.156 cm<sup>3</sup> g<sup>-1</sup> for Fe<sub>3</sub>O<sub>4</sub>@mSiO<sub>2</sub>-P7250, 100 m<sup>2</sup> g<sup>-1</sup> and 0.133 cm<sup>3</sup> g<sup>-1</sup> for Fe<sub>3</sub>O<sub>4</sub>@mSiO<sub>2</sub>-P8750, 68.0 m<sup>2</sup> g<sup>-1</sup> and 0.095 cm<sup>3</sup> g<sup>-1</sup> for Fe<sub>3</sub>O<sub>4</sub>@mSiO<sub>2</sub>-P10000 (Table 1).

The magnetization characterization of the samples was also studied. Fig. 4 presents the magnetic hysteresis loop of Fe<sub>3</sub>O<sub>4</sub> and Fe<sub>3</sub>O<sub>4</sub>@mSiO<sub>2</sub>-P(EO-co-LLA) at room temperature. In Fig. 4, Fe<sub>3</sub>O<sub>4</sub> nanoparticles possess magnetism with the saturation magnetizations ( $M_s$ ) about 80.5 emu g<sup>-1</sup>. Fe<sub>3</sub>O<sub>4</sub>@mSiO<sub>2</sub>-P(EO-co-LLA)s has super-paramagnetism with the reduced  $M_s$  about 59.5, 55.6, and 48.7 emu g<sup>-1</sup>, which is ascribed to the nonmagnetic mSiO<sub>2</sub> and P(EO-co-LLA).

### Drug loading and release profiles

To investigate the sensitive and controlled release properties of Fe<sub>3</sub>O<sub>4</sub>@mSiO<sub>2</sub>-P(EO-co-LLA)s, DOX was selected as the model drug and the release performances were investigated in detail (Table 1). The actual loading levels of DOX were calculated to be 6.8 ± 0.5, 6.2 ± 0.6 and 5.9 ± 0.4% with the increase of the corresponding molecular weight of P(EO-co-LLA)s from 7250 to 8750 and 10 000, respectively. It is known that the drug loading ability is related to the surface area of carriers. With a large surface area, Fe<sub>3</sub>O<sub>4</sub>@mSiO<sub>2</sub>-P7250 (152 m<sup>2</sup> g<sup>-1</sup>) possesses a high drug loading amount (6.8 ± 0.5%).

The release profiles of DOX-Fe<sub>3</sub>O<sub>4</sub>@mSiO<sub>2</sub>-P(EO-co-LLA)s in PBS buffer (pH 7.4) in response to the temperature (20 and 45 °C) are shown in Fig. 5A. In Fig. 5A(d and e), all samples show low release cumulative amounts (below 10%) until 24 h

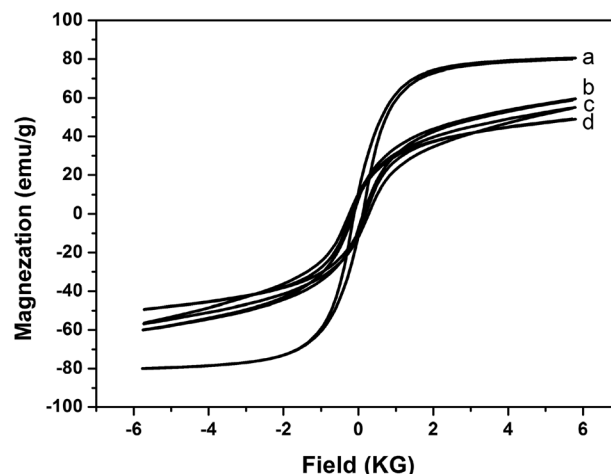


**Fig. 4** Representative hysteresis-loop measurements of the obtained a: Fe<sub>3</sub>O<sub>4</sub>@mSiO<sub>2</sub>, b: Fe<sub>3</sub>O<sub>4</sub>@mSiO<sub>2</sub>-P7250, c: Fe<sub>3</sub>O<sub>4</sub>@mSiO<sub>2</sub>-P8750 and d: Fe<sub>3</sub>O<sub>4</sub>@mSiO<sub>2</sub>-P10000.

at a low temperature (25 °C). However, the release became more easy when the temperature was increased to 45 °C. In Fig. 5A(a-c), the cumulative release amount of DOX reaches 24.7, 28.6 and 38.0% for DOX-Fe<sub>3</sub>O<sub>4</sub>@mSiO<sub>2</sub>-P7250, DOX-Fe<sub>3</sub>O<sub>4</sub>@mSiO<sub>2</sub>-P8750 and DOX-Fe<sub>3</sub>O<sub>4</sub>@mSiO<sub>2</sub>-P10000 within 24 h, respectively. With a higher molecular weight of the polymer, DOX-Fe<sub>3</sub>O<sub>4</sub>@mSiO<sub>2</sub>-P10000 shows a higher release amount (38.0%).

Considering the pH-sensitivity of P(EO-co-LLA), the release profile of DOX-Fe<sub>3</sub>O<sub>4</sub>@mSiO<sub>2</sub>-P10000 was also studied under different pH conditions (pH 7.4, 5.8 and 4.0). In Fig. 5B, the fast burst release can be found at pH 4. It just takes 24 h to reach maximum release (92.7%). However, when the pH value increases to 5.8, the release rate decreases as well as the release amount. Fig. 5B shows about 89.4% release amount until 24 h at pH 5.8. Going on to increase the pH value to 7.4, the release decreases more obviously (38.0%). From the above, the acidic condition is beneficial for the drug release. Comparing the release profiles in Fig. 5B and C, it can be also found that the release at 45 °C is freer than that at 25 °C.

To further reveal the sensitive-release mechanism of the system, the hydrodynamic sizes of all samples under different temperatures/pH values/molecular amounts were investigated and are summarized in Table 2. As can be seen in Table 2, as the molecular amount of P(EO-co-LLA)s increases from 7250 to 8750 and 10 000, the hydrodynamic size of Fe<sub>3</sub>O<sub>4</sub>@mSiO<sub>2</sub>-P(EO-co-LLA)s increases from 108 to 149 nm at pH 7.4 (25 °C).

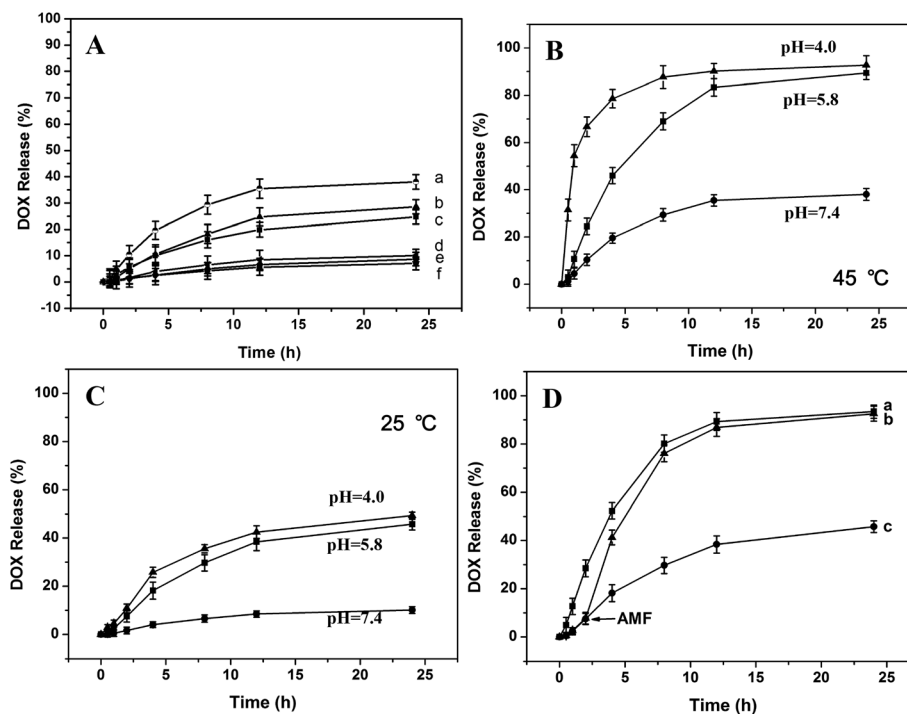


**Fig. 5** (A) Release profiles of DOX from  $\text{Fe}_3\text{O}_4@\text{mSiO}_2\text{-P10000}$  (a: 45 °C and f: 25 °C),  $\text{Fe}_3\text{O}_4@\text{mSiO}_2\text{-P8750}$  (b: 45 °C and e: 25 °C),  $\text{Fe}_3\text{O}_4@\text{mSiO}_2\text{-P7250}$  (c: 45 °C and d: 25 °C) at pH 7.4. Release profiles of DOX from  $\text{Fe}_3\text{O}_4@\text{mSiO}_2\text{-P10000}$  under different pH conditions at 45 °C (B) and 25 °C (C). (D) Release profiles of DOX from  $\text{Fe}_3\text{O}_4@\text{mSiO}_2\text{-P10000}$  (pH 5.8) a: with AMF from  $t = 0$  h, b: with AMF from  $t = 2$  h, and c: without AMF.

**Table 2** The hydrodynamic size of the samples

Samples	$T = 25$ °C	$T = 45$ °C
DOX- $\text{Fe}_3\text{O}_4@\text{mSiO}_2\text{-P7250}$ (pH 5.8)	97 nm	85 nm
DOX- $\text{Fe}_3\text{O}_4@\text{mSiO}_2\text{-P7250}$ (pH 7.4)	108 nm	102 nm
DOX- $\text{Fe}_3\text{O}_4@\text{mSiO}_2\text{-P8750}$ (pH 5.8)	115 nm	97 nm
DOX- $\text{Fe}_3\text{O}_4@\text{mSiO}_2\text{-P8750}$ (pH 7.4)	130 nm	122 nm
DOX- $\text{Fe}_3\text{O}_4@\text{mSiO}_2\text{-P10000}$ (pH 4.0)	128 nm	99 nm
DOX- $\text{Fe}_3\text{O}_4@\text{mSiO}_2\text{-P10000}$ (pH 5.8)	131 nm	105 nm
DOX- $\text{Fe}_3\text{O}_4@\text{mSiO}_2\text{-P10000}$ (pH 7.4)	149 nm	138 nm

With the high molecular amount of P(EO-co-LLA), the corresponding hydrodynamic size increases due to the long chain of the polymer brushes that makes the release amount decrease from 10.1% of DOX- $\text{Fe}_3\text{O}_4@\text{mSiO}_2\text{-P7250}$  to 7.1% of DOX- $\text{Fe}_3\text{O}_4@\text{mSiO}_2\text{-P10000}$  (Fig. 5A).

It is known that P(EO-co-LLA) is a typical temperature sensitive polymer, which can change from sol to gel as the temperature increases above its lower critical solution temperature (LCST). As displayed in Table 2, when the temperature increases to 45 °C, the hydrodynamic size of  $\text{Fe}_3\text{O}_4@\text{mSiO}_2\text{-P(EO-co-LLA)}$ s decreases to 102, 122, and 138 nm (pH 7.4) due to the shrinking of the polymer brushes at high temperature. In short, when the temperature increases to 45 °C, all the releases were accelerated and the release amount increased obviously, while at 25 °C, the loose polymer brushes block the pore and make the release below 10%. Furthermore, the shrinking/loosening of polymer brushes based on temperature

takes place not only at pH 7.4, but also at pH 5.8 and 4.0 (Table 2).

As mentioned above, besides the temperature-triggered release, DOX- $\text{Fe}_3\text{O}_4@\text{mSiO}_2\text{-P10000}$  reveals also pH sensitive-release behavior under different pH conditions. It is known that the swelling of P(EO-co-LLA) in aqueous solution depends on the hydrogen bond between P(EO-co-LLA) and  $\text{H}_2\text{O}$ . When decreasing the pH value of the solution, the hydrogen bond is weakened, leading to the shrinking of polymer brushes. As illustrated in Table 2, as the pH value decreases from 7.4 to 5.8 and 4.0, the hydrodynamic size of DOX- $\text{Fe}_3\text{O}_4@\text{mSiO}_2\text{-P10000}$  decreases from 149 to 131 and 128 nm at 25 °C and from 138 to 105 and 99 nm at 45 °C. So, the shrinking of P(EO-co-LLA) makes the preponderant release in the acidic environment as depicted in Fig. 5B and C.

From the above investigation, the temperature-triggered release behavior of the nanocomposites is very definite. Considering the hyperthermia of the magnetic  $\text{Fe}_3\text{O}_4$ , AMF was also introduced to control the release process and the release performances. As shown in Fig. 5D, under the stimulus of AMF, the release is enhanced to 28.7% at 2 h and 89.4% at 12 h. To further reveal the AMF enhanced release, the release without AMF firstly and then with AMF was also carried out. The release is very slow (about 7.8%) at the first 2 h. Then, AMF was introduced and the release increased to 41.3% at 4 h and even 86.8% at 12 h. In addition, the time-dependent temperature of  $\text{Fe}_3\text{O}_4@\text{mSiO}_2\text{-P10000}$  under AMF treatment is shown in Fig. S4.† After AMF treatment for 10 min, the temp-

erature increases to 35 °C. It costs about 20 min to reach 45 °C. As time goes on, the temperature can reach 47 °C under the AMF stimulus for 30 min. In Fig. 5D and S4,† AMF stimuli-release can be ascribed to the hyperthermia of the magnetic  $\text{Fe}_3\text{O}_4$  that causes the temperature increase and drug release.

### *In vitro* cytotoxic effect and cellular uptake

To investigate the cellular uptake of the sample, DOX- $\text{Fe}_3\text{O}_4$ @mSiO<sub>2</sub>-P10000 was incubated with HeLa cells at a concentration of 100  $\mu\text{g mL}^{-1}$  for 6 h. The cellular uptake and subsequent localization of the sample is shown in Fig. 6. As can be seen in Fig. 6, nanoparticles are localized in the cytoplasm after 6 h of incubation, proving the fast cellular uptake of the sample. In addition, DOX can be found in karyon that is because the nanocomposites were taken into the cytoplasm and the low-pH endosomal environment induced the drug release.<sup>15</sup>

To compare the anticancer efficacy of the DOX-loaded nanocomposites and free DOX, HeLa cells were incubated in culture medium in the presence of free DOX,  $\text{Fe}_3\text{O}_4$ @mSiO<sub>2</sub>-P10000 and DOX- $\text{Fe}_3\text{O}_4$ @mSiO<sub>2</sub>-P10000 with various concentrations for 48 h, and then the MTT assay was used for quantitative testing of the cell viability. As shown in Fig. 7A,  $\text{Fe}_3\text{O}_4$ @mSiO<sub>2</sub>-P10000 shows a high cell viability (89.5%) even after 48 h of incubation, with the sample concentration as high as 480  $\mu\text{g mL}^{-1}$ , showing the neglectable toxicity and good biocompatibility of the nanocomposites. However, the cell viability decreases to 62.7% (480  $\mu\text{g mL}^{-1}$ ) due to the hyperthermia of the magnetic nanocomposites under AMF treatment (Fig. 7A).

In Fig. 7B, DOX- $\text{Fe}_3\text{O}_4$ @mSiO<sub>2</sub>-P10000 exhibits 71.5% apoptosis at an equivalent DOX concentration of 50  $\mu\text{g mL}^{-1}$ . Assisted with AMF stimuli, the cellular apoptosis is enhanced to 93.7%, revealing that the chemotherapy combined with hyperthermia can improve the cellular cytotoxicity obviously.

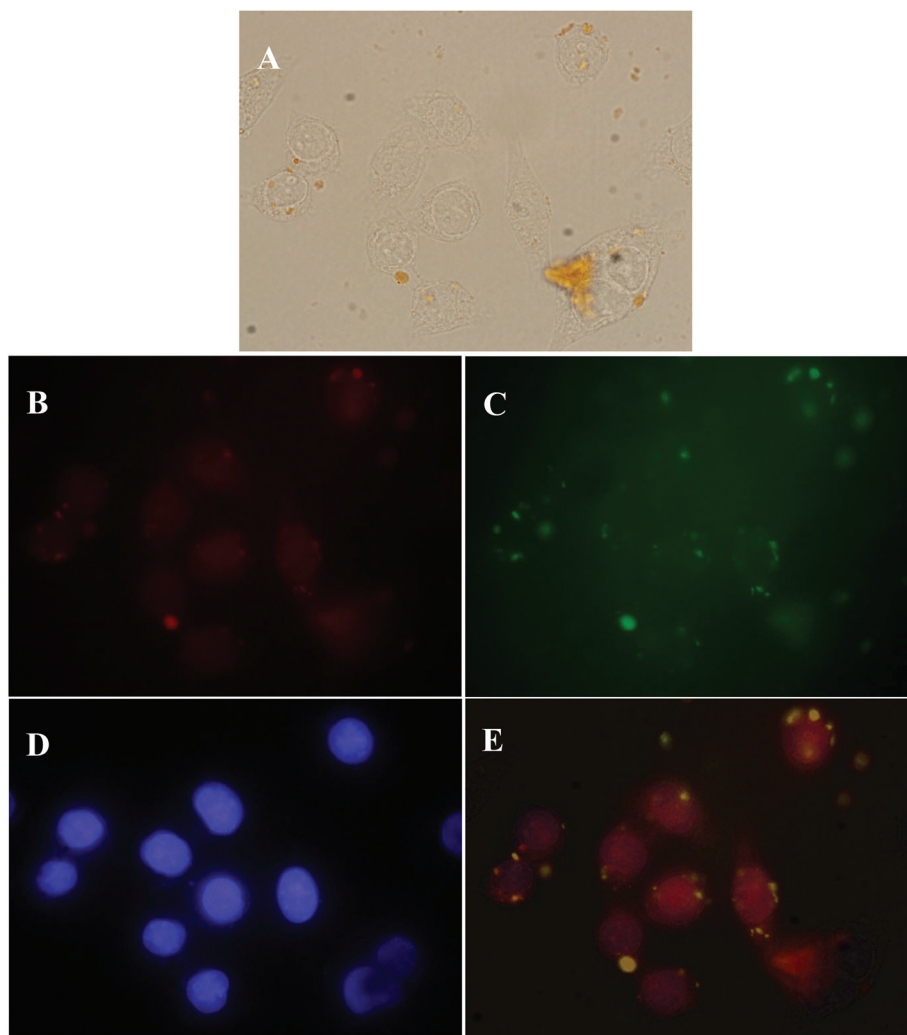


**Fig. 6** CLSM images of HeLa cells after incubation with 100  $\mu\text{g mL}^{-1}$  of DOX- $\text{Fe}_3\text{O}_4$ @mSiO<sub>2</sub>-P10000 for 6 h. (A) HeLa cells (bright), (B) DOX fluorescence in cells (red), (C) FITC labeled DOX- $\text{Fe}_3\text{O}_4$ @mSiO<sub>2</sub>-P10000 (green), (D) Hoechst 33342 labeled cell nucleus (blue), and (E) merged.



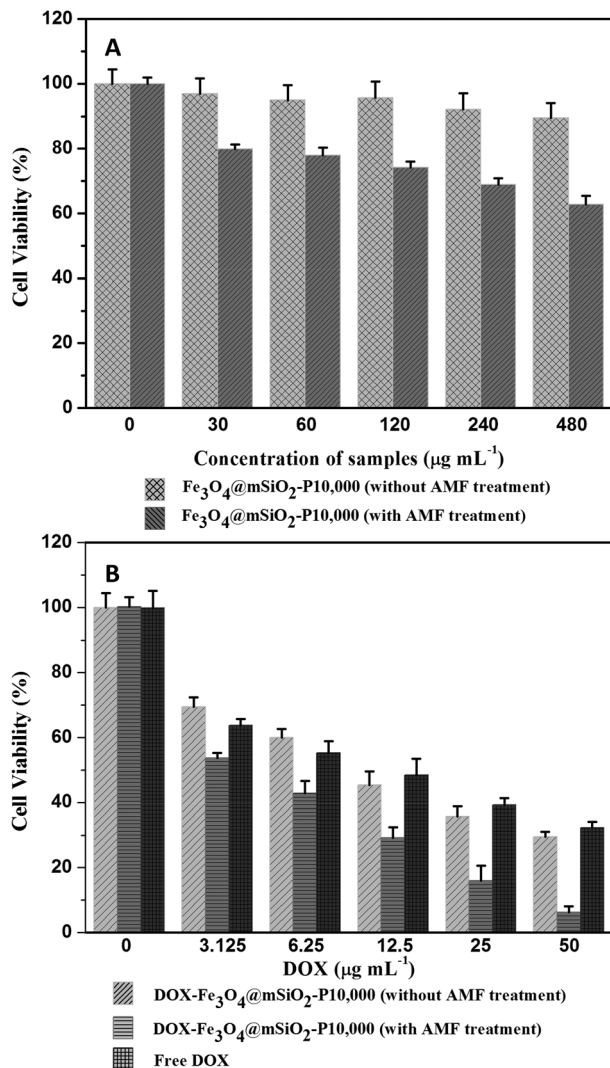


Fig. 7 Cell viability of HeLa cells incubated with different amounts of (A)  $\text{Fe}_3\text{O}_4@\text{mSiO}_2\text{-P10000}$ ,  $\text{Fe}_3\text{O}_4@\text{mSiO}_2\text{-P10000}$  with AMF, and (B) DOX- $\text{Fe}_3\text{O}_4@\text{mSiO}_2\text{-P10000}$ , DOX- $\text{Fe}_3\text{O}_4@\text{mSiO}_2\text{-P10000}$  with AMF, and free DOX.

Furthermore, free DOX exhibits slightly higher cytotoxicity than DOX- $\text{Fe}_3\text{O}_4@\text{mSiO}_2\text{-P10000}$  in the low concentrations region. However, this was inverted when the concentration of DOX is up to  $12.5 \mu\text{g mL}^{-1}$ . Because small molecules like DOX can diffuse into cells rapidly, that induces the high cytotoxicity for free DOX at low concentration. Whereas the cytotoxicity of DOX- $\text{Fe}_3\text{O}_4@\text{mSiO}_2\text{-P10000}$  derived from the released DOX molecules after endocytic uptake by cancer cells.<sup>46</sup> At high concentration, the high uptake of the nanocomposites by HeLa cells through endocytosis, followed by the low-pH induced release of the loaded DOX inside the endosomal compartment, make the cytotoxicity of DOX- $\text{Fe}_3\text{O}_4@\text{mSiO}_2\text{-P10000}$  higher than that of free DOX molecules. In addition, the chemotherapy combined with the hyperthermia makes DOX- $\text{Fe}_3\text{O}_4@\text{mSiO}_2\text{-P10000}$  show the obviously enhanced cyto-

toxicity (93.7%) as an equivalent DOX (87.4%) concentration of  $50 \mu\text{g mL}^{-1}$ .

## Conclusion

In summary,  $\text{Fe}_3\text{O}_4@\text{mSiO}_2$  core-shell nanocomposites were synthesized as the nanocarriers. Considering the magnetic hyperthermia of  $\text{Fe}_3\text{O}_4$  under AMF, a thermo-sensitive polymer P(EO-co-LLA) was used as “gatekeeper” coating outside  $\text{Fe}_3\text{O}_4@\text{mSiO}_2$  to regulate the drug release behavior. After the loading of the anticancer drug DOX, the composites show controlled drug release behavior triggered by the hyperthermia of  $\text{Fe}_3\text{O}_4$  under AMF. Besides this, the nanocarriers also demonstrate the pH-sensitive control release based on the slight acidity difference between the tumor and the normal tissue. The chemotherapy of the anticancer drug combined with magnetic hyperthermia enhances the cytotoxicity obviously. Therefore, with these unique properties, the nanocomposites have potential applications in targeted-control drug release and hyperthermia for cancer therapy.

## Acknowledgements

Financial support for this study was provided by the National Natural Science Foundation of China (21471041, 21171045, 21101046, 21441002), Natural Science Foundation of Heilongjiang Province of China (ZD201214), Technology development pre-project of Harbin Normal University (12XYG-11).

## References

- 1 B. Fischer, P. Heffeter, K. Kryeziu, L. Gille, S. M. Meier, W. Berger, C. R. Kowol and B. K. Keppler, *Dalton Trans.*, 2014, **43**, 1096.
- 2 J. Wu, Y. J. Zhu, F. Chen, X. Y. Zhao, J. Zhao and C. Qi, *Dalton Trans.*, 2013, **42**, 7032.
- 3 X. Q. An, F. Zhan and Y. Y. Zhu, *Langmuir*, 2013, **29**, 1061.
- 4 J. C. Fernandes, X. P. Qiu, F. M. Winnik, M. Benderdour, X. Zhang, K. Dai and Q. Shi, *Int. J. Nanomed.*, 2012, **7**, 5833.
- 5 A. Shimoda, S. I. Sawada, A. Kano, A. Maruyama, A. Moquin, F. M. Winnik and K. Akiyoshi, *Colloids Surf., B*, 2012, **99**, 38.
- 6 E. R. Gillies and J. M. Fréchet, *Drug Discovery Today*, 2005, **10**, 35.
- 7 M. Colilla, B. González and M. Vallet-Regí, *Biomater. Sci.*, 2013, **1**, 114.
- 8 M. Vallet-Regí and E. Ruiz-Hernández, *Adv. Mater.*, 2011, **23**, 5177.
- 9 J. Chang, Y. Li, G. Wang, B. He and Z. W. Gu, *Nanoscale*, 2013, **5**, 813.
- 10 A. H. Faraji and P. Wipf, *Bioorg. Med. Chem.*, 2009, **17**, 2950.

- 11 H. Y. Chen, B. W. Li, J. D. Qiu, J. Y. Li, J. Jin, S. H. Dai, Y. X. Ma and Y. Q. Gu, *Nanoscale*, 2013, **5**, 12409.
- 12 H. Kim, S. Kim, C. Park, H. Lee, H. J. Park and C. Kim, *Adv. Mater.*, 2010, **22**, 4280.
- 13 Y. N. Zhao, B. G. Trewyn, I. I. Slowing and V. S.-Y. Lin, *J. Am. Chem. Soc.*, 2009, **131**, 8398.
- 14 H. S. Park, C. W. Kim, H. J. Lee, J. H. Choi, S. G. Lee, Y. P. Yun, I. C. Kwon, S. J. Lee, S. Y. Jeong and S. C. Lee, *Nanotechnology*, 2010, **21**, 225101.
- 15 L. Yuan, Q. Tang, D. Yang, J. Z. Zhang, F. Zhang and J. Hu, *J. Phys. Chem. C*, 2011, **115**, 9926.
- 16 X. F. Guo, Y. S. Kim and G. J. Kim, *J. Phys. Chem. C*, 2009, **113**, 8313.
- 17 X. Zhang, P. P. Yang, Y. L. Dai, P. A. Ma, X. J. Li, Z. Y. Cheng, Z. Y. Hou, X. J. Kang, C. X. Li and J. Lin, *Adv. Funct. Mater.*, 2013, **23**, 4067.
- 18 Z. Li, J. L. Nyalosaso, A. A. Hwang, D. P. Ferris, S. Yang, G. Derrien, C. Charnay, J. O. Durand and J. I. Zink, *J. Phys. Chem. C*, 2011, **115**, 19496.
- 19 J. T. Sun, C. Y. Hong and C. Y. Pan, *J. Phys. Chem. C*, 2010, **114**, 12481.
- 20 M. W. Ambrogio, C. R. Thomas, Y.-L. Zhao, J. I. Zink and J. F. Stoddart, *Acc. Chem. Res.*, 2011, **44**, 903.
- 21 S. Angelos, N. M. Khashab, Y. W. Yang, A. Trabolsi, H. A. Khatib, J. F. Stoddart and J. I. Zink, *J. Am. Chem. Soc.*, 2009, **131**, 12912.
- 22 D. P. Ferris, Y. L. Zaho, N. M. Khashab, H. A. Khatib, J. F. Stoddart and J. I. Zink, *J. Am. Chem. Soc.*, 2009, **131**, 1686.
- 23 E. Aznar, M. D. Marcos, R. Martinez-Manez, F. Sancenon, J. Soto, P. Amoros and C. Guillem, *J. Am. Chem. Soc.*, 2009, **131**, 6833.
- 24 Y. Zhu, W. Meng, H. Gao and N. Hanagata, *J. Phys. Chem. C*, 2011, **115**, 13630.
- 25 S. Angelos, E. Choi, F. Vögtle, L. De Cola and J. I. Zink, *J. Phys. Chem. C*, 2007, **111**, 6589.
- 26 X. R. Zhang, D. Chabot, Y. Sultan, C. Monreal and M. C. DeRosa, *ACS Appl. Mater. Interfaces*, 2013, **5**, 5500.
- 27 A. Rodríguez-Pulido, A. I. Kondrachuk, D. K. Prusty, J. Gao, M. A. Loi and A. Herrmann, *Angew. Chem., Int. Ed.*, 2013, **52**, 1008.
- 28 W. Guo, C. Y. Yang, L. R. Cui, H. M. Lin and F. Y. Qu, *Langmuir*, 2014, **30**, 243.
- 29 R. Weissleder, A. Bogdanov, E. A. Neuwelt and M. Papisov, *Adv. Drug Delivery Rev.*, 1995, **16**, 321.
- 30 J. Su, M. Cao, L. Ren and C. Hu, *J. Phys. Chem. C*, 2011, **115**, 14469.
- 31 X. Li, X. Huang, D. Liu, X. Wang, S. Song, L. Zhou and H. Zhang, *J. Phys. Chem. C*, 2011, **115**, 21567.
- 32 R. Xu, G. Y. Sun, Q. Y. Li, E. B. Wang and J. M. Gu, *Solid State Sci.*, 2010, **12**, 1720.
- 33 E. Taboada, E. Rodríguez, A. Roig, J. Oró, A. Roch and R. N. Muller, *Langmuir*, 2007, **23**, 4583.
- 34 V. Rocher, J. Manerova, M. Kinnear, D. J. Evans and M. G. Francesconi, *Dalton Trans.*, 2014, **43**, 2948.
- 35 T. D. Schladt, K. Schneider, H. Schild and W. Tremel, *Dalton Trans.*, 2011, **40**, 6315.
- 36 A. Ito, Y. K. Honda, H. Kikkawa, A. Horiuchi, Y. Watanabe and T. Kobayashi, *Cancer Lett.*, 2004, **212**, 167.
- 37 A. A. Luderer, N. F. Borrelli, J. N. Panzarino, G. R. Mansfield, D. M. Hess, J. L. Brown, E. H. Bamett and E. W. Hahn, *Radiat. Res.*, 1983, **94**, 190.
- 38 W. C. Dewey, *Int. J. Hyperthermia*, 1994, **10**, 457.
- 39 W. W. He, L. Cheng, L. F. Zhang, Z. Liu, Z. P. Cheng and X. L. Zhu, *Polym. Chem.*, 2014, **5**, 638.
- 40 N. A. Brusentsov, V. V. Gogosov, T. N. Brusentsov, A. V. Sergeev, N. Y. Jurchenko, A. A. Kuznetsov, O. A. Kuznetsov and L. I. Shumukov, *J. Magn. Magn. Mater.*, 2001, **225**, 113.
- 41 A. Baeza, E. Guisasola, E. Ruiz-Hernández and M. Vallet-Regí, *Chem. Mater.*, 2012, **24**, 517.
- 42 X. Zhang, P. P. Yang, Y. L. Dai, P. A. Ma, X. J. Li, Z. Y. Cheng, Z. Y. Hou, X. J. Kang, C. X. Li and J. Lin, *Adv. Funct. Mater.*, 2013, **23**, 4067.
- 43 B. Jeong, Y. H. Bae, D. S. Lee and S. W. Kim, *Nature*, 1997, **388**, 860.
- 44 J. Park, K. An, Y. H. Wang, J. G. Park, H. J. Noh, J. Y. Kim and T. Hyeon, *Nat. Mater.*, 2004, **3**, 891.
- 45 B. Jeong, D. S. Lee and J. I. Shon, *J. Polym. Sci., Part A: Polym. Chem.*, 1999, **37**, 751.
- 46 J. Chen, X. Z. Qiu, J. Ouyang, J. M. Kong, W. Zhong and M. M. Q. Xing, *Biomacromolecules*, 2011, **12**, 3601.